ChemComm

COMMUNICATION

View Article Online
View Journal | View Issue

Cite this: *Chem. Commun.*, 2020, **56**, 14817

Received 9th September 2020,
Accepted 27th October 2020

DOI: 10.1039/d0cc06092e

rsc.li/chemcomm

Axial Cl/Br atom-mediated CO_2 electroreduction performance in a stable porphyrin-based metal–organic framework†

Qing Huang,[a] Qian Niu,[b] Na-Na Ma,[c] Long-Zhang Dong,[b] Shun-Li Li,*[b] Dong-Sheng Li,[d] Yue-Peng Cai[a] and Ya-Qian Lan*[ab]

Two isostructural MOFs with coordination of different halogen ions (Cl^- and Br^-), namely NNU-17 and NNU-18, were utilized to reveal the influence of different electron-withdrawing halogen anions on ECR performance. The performance difference between them mainly originates from the different abilities of adsorption and activation of CO_2 by halogen ions.

Excessive CO_2 emissions have caused severe climate change and environmental crises. Electrocatalytic CO_2 reduction (ECR) is one of the most promising methods for carrying out carbon cycling.[1] However, the chemical adsorption and activation of CO_2 molecule are very difficult due to its inherent chemical inertness. There are many studies devoted to adjusting the halogen ions near/on the surface of the catalyst to promote the CO_2 reduction reaction.[2–6] Previous ECR studies have shown that the adsorption of halogen ions on the catalyst in halide electrolyte can inhibit the adsorption of protons and lead to a higher overpotential for hydrogen production.[2] Moreover, the halogen ions would be adsorbed on the surface of the Cu electrode after they were added to the electrolyte, these specifically adsorbed halide anions would transfer electrons to the vacant orbital of CO_2 through $X_{ad}{}^-$(Br^-, Cl^-, I^-)–C bond, thereby activating the CO_2 molecule to promote the electrocatalytic reduction of CO_2. Similar work, by adding different halogen ions in the electrolyte, explored the influence of halide types on promoting ECR reaction efficiency.[3] Some studies have found that the special adsorption of halide ions on the surface of polycrystalline copper helped the formation and stabilization of carboxyl intermediates.[4] Furthermore, Cl^- ions are directly electrodeposited on the surface of metal nanoparticles (NPs), and the reduction of CO_2 to CO is promoted by the van der Waals force between the key intermediates and adsorbed Cl^- ions.[5] Another work prepared Cl-modified surface of Ag nanomaterials (Ag–Cl NPs) for further ECR reaction.[6] The XANES and XPS analysis showed that the Ag–Cl NPs electrode with surface Cl^- adsorption exhibited the high catalytic activity by strengthening the interaction with CO_2, accelerating the process of proton-coupled electron transfer and promoting the activation of CO_2 molecules. Therefore, it is reasonably believed that the adsorbed halogen ions can improve the catalytic efficiency of CO_2 reduction. If the halogen ions can be directly coordinated on catalyst, the activity would be enhanced significantly, moreover, a structure model of halogen-coordinated MOF catalyst can thus be established for further exploring the adsorption and activation of CO_2 molecules.

Metal organic frameworks (MOFs) are periodically arranged crystalline porous materials composed of metal ions/clusters and organic ligands,[7,8] as well as a good structural model. They have emerged as a kind of crystalline heterogeneous catalyst thanks to the inherent porosity and clear active site.[9–11] The large specific surface area of MOFs is conducive to the adsorption of CO_2 molecules and the enhancement of fast mass transfer ability,[12–14] thereby playing a critical role in ECR reaction. Moreover, the well-defined MOF can provide visual research platform for the reaction mechanism, which can be used as a structural model to investigate separate and combined effects of catalytic center, the specific functional groups, and coordination environments in the ECR reaction.[15,16] The present ECR electrocatalysts of pristine MOFs are also relatively limited, (*e.g.* [$Al_2(OH)_2$(Co(tcpp))], Fe-MOF-525 and ZIF-8 systems), mainly involving the influence of different metal active sites or different ligand of functional groups on the ECR performance.[15,17–19] However, there is currently no precise structural model to investigate the

[a] *Department of Chemistry, South China Normal University, Guangzhou, 510006, China. E-mail: yqlan@njnu.edu.cn*
[b] *School of Chemistry and Materials Science, Nanjing Normal University, Nanjing, 210023, China. E-mail: slli@njnu.edu.cn*
[c] *School of Chemistry and Chemical Engineering, Henan Normal University, Xinxiang, 453007, China. E-mail: mann076@htu.edu.cn*
[d] *College of Materials and Chemical Engineering, China Three Gorges University, Yichang, 443002, China*

† Electronic supplementary information (ESI) available. CCDC 1993105 and 1993106. For ESI and crystallographic data in CIF or other electronic format see DOI: 10.1039/d0cc06092e

effect of halogen ions on the adsorption and activation of CO_2 molecules in ECR reaction.

Herein, we synthesized two stable isostructural MOFs, [$(CdCl_{1.3}(OH)_{0.7}$(Cd-TIPP))] and [$CdBr_{1.3}(OH)_{0.7}$(Cd-TIPP)], namely NNU-17 and NNU-18. Cl/Br anions were modulated directly to coordinate with metal ions, and to further reveal the effect of different halogen anions on ECR performance. The maximum faradaic efficiency for CO (FE_{CO}) of NNU-17 can reach 90.3% at −1.0 V *vs.* reversible hydrogen electrode (RHE), while that of NNU-18 is 62.5%. The maximum FE_{CO} of NNU-17 is a bit higher than that of NNU-18 (82.1%) appearing at −1.1 V. The results of CO_2 adsorption show that the adsorption capacity of NNU-17 (76.1 $cm^3\ g^{-1}$) is three times higher than that of NNU-18 (24.5 $cm^3\ g^{-1}$). The DFT calculations exhibit a curved state of CO_2 along with the stronger CO_2 binding energy on coordinated Cl^- than on Br^-. The calculated interaction energy implies that the former may have a stronger affinity for CO_2 during ECR process.

NNU-17 (or NNU-18) was synthesized as dark violet plate crystals *via* DMF–water mixed solvothermal reaction of TIPP and $CdCl_2$ (or $CdBr_2$) (Fig. S1 and S2, ESI†). Single-crystal X-ray diffraction analysis reveals that NNU-17 is isostructural to NNU-18 and they crystallize in the orthorhombic space group *Cmca* with chemical formula [$CdCl_{1.3}(OH)_{0.7}$(Cd-TIPP)$_2$] and [$CdBr_{1.3}(OH)_{0.7}$(Cd-TIPP)$_2$] respectively (Table S1, ESI†). Both NNU-17 and NNU-18 are 2D layered structures established by TIPP ligand and Cd ions (Fig. 1). There are two different coordination conditions situations for Cd ions in the NNU-17 structure. One is that each Cd2 ion is coordinated by the imidazole groups from four TIPPs and two Cl ions (Fig. 1a and Fig. S3, ESI†), the other is that each Cd1 ion is trapped in the center of porphyrin and simultaneously docked by imidazole N of another TIPP ligand (Fig. 1b and Fig. S4, ESI†). Only three imidazole groups of each Cd-TIPP ligand are coordinated to Cd^{2+} ions as well as keeping one uncoordinated imidazole group (N10), in which two adjacent imidazole groups (N1 and N4) are coordinated to two Cd2 ions and the other N atom (N7) is coordinated to the Cd1 ion (Fig. S4, ESI†). Based on above coordination mode, each TIPP connects Cd1 and Cd2 to form a 2D layered structure (Fig. 1b–d). As a result, a 2D + 2D → 3D interdigitated architecture is accomplished by intermolecular force (Fig. 1e, f and Fig. S5, S6, ESI†). As the isostructural characters, NNU-18 has the similar coordination mode between ligand and Cd ions but with a slight difference: the position of Cl^- is occupied by Br^- (Fig. 1b and Fig. S3–S7, ESI†).

The phase purity of crystal samples was verified by powder X-ray diffraction (PXRD) patterns (Fig. S8, ESI†). Thermogravimetric analysis (TGA) under O_2 atmosphere shows that the first mass loss is about 10%, which can be attributed to the solvent molecules of NNU-17 structures, followed by a stable platform until the skeleton starts collapsed around 330 °C, yielding CdO at higher temperatures (Fig. S9, ESI†). In contrast to NNU-17, a similar TGA pattern of NNU-18 indicates that NNU-18 is thermally stable up to 330 °C. Therefore, both NNU-17 and NNU-18 exhibit good thermal stability under O_2 atmosphere. Poor acid and alkali resistance might inhibit the stability of MOFs in aqueous. Thus, the experiments on investigating acid and alkali resistance of NNU-17 and NNU-18 were conducted by immersing them in various solutions under wide range of pH values.

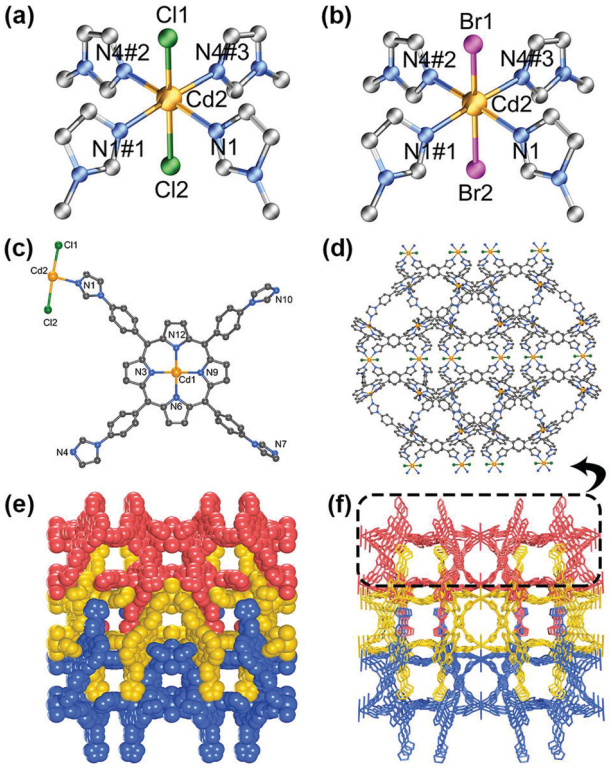

Fig. 1 The crystal structure of NNU-17 and NNU-18: the difference of Cd2 coordination environment between (a) NNU-17 and (b) NNU-18; (c) the asymmetric unit of NNU-17; (d) the 2D structure of NNU-17; (e) the space-filling model of NNU-17; (f) the 2D + 2D → 3D interdigitated architecture; for the sake of clarity, the H atom and the occupied O atom next to Cl2/Br2 are not shown. Color code: C, black; N, blue; Cl, green; Br: rose red; Cd: golden. Symmetric codes: # 1 1 − *x*, *y*, *z*; # 2 1 − *x*, 1 − *y*, 1 − *z*; # 3 *x*, 1 − *y*, 1 − *z*.

After 24 hours, there is no obvious difference in the PXRD patterns before and after immersion (Fig. S8, ESI†), confirming that these samples can maintain structural integrity in both solutions with a wide pH range of 3–12 and 0.5 M $KHCO_3$. NNU-17 and NNU-18 exhibit the excellent acid and alkali resistance, which is a prerequisite for the electrocatalyst to perform CO_2 reduction reaction. The CO_2 sorption properties of NNU-17 and NNU-18 were assessed at 273 K and 298 K, respectively. The maximum CO_2 adsorption capacity of NNU-17 can reach to 76.1 $cm^3\ g^{-1}$ and 56.0 $cm^3\ g^{-1}$, respectively, while the maximum CO_2 adsorption capacity of NNU-18 is only 24.5 $cm^3\ g^{-1}$ and 19.1 $cm^3\ g^{-1}$ (Fig. S10, ESI†). With stronger adsorption capacity of CO_2, the NNU-17, have the potential to show more excellent performance of ECR reaction than NNU-18.

Linear scanning voltammetry (LSV) experiments were conducted to evaluate the ECR performance in the 0.5 M $KHCO_3$ solution saturated with CO_2/Ar. In this work, all the experiments were carried out *vs.* Ag/AgCl electrode and the potential results were recorded *vs.* RHE. For NNU-17 and NNU-18, the current density obtained under a CO_2-saturated 0.5 M $KHCO_3$ aqueous solution (aq) is higher than that generated under Ar-saturated $KHCO_3$ (aq), which shows that both of them have the ability to electroreduction CO_2 (Fig. S11, ESI†). Under CO_2-saturated $KHCO_3$ (aq), the onset potential of NNU-17 is −0.47 V, which is more positive than that of

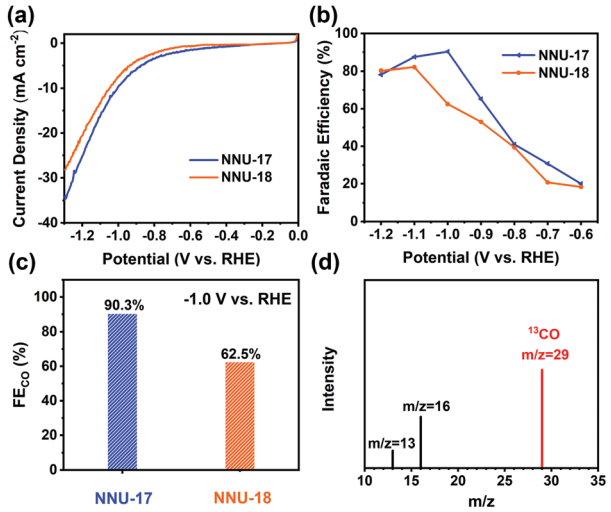

Fig. 2 Electrocatalytic performances of NNU-17 and NNU-18. (a) Linear sweep voltammetric curves of NNU-17 and NNU-18 in CO_2-saturated 0.5 M $KHCO_3$ aqueous solution (pH = 7.2). (b) FE_{CO} of NNU-17 and NNU-18 at various applied potentials in CO_2-saturated 0.5 M $KHCO_3$ aqueous solution. (c) FE_{CO} of NNU-17 and NNU-18 at −1.0 V. (d) Gas chromatography-mass spectra of ^{13}CO recorded under a $^{13}CO_2$ atmosphere.

NNU-18 (−0.68 V). And the current density of NNU-17 at −1.3 V (35.7 mA cm^{-2}) is much higher than that of NNU-18 (28.2 mA cm^{-2}) (Fig. 2a).

In order to determine the products of ECR, the electrolysis reactions were performed in CO_2-saturated 0.5 M $KHCO_3$ (aq). H_2 and CO were detected by gas chromatography (GC) as the major reduction products (Fig. S12, ESI†), with a total FE of approximately 100% (Fig. 2b and Fig. S13, ESI†). The results of the ^{1}H nuclear magnetic resonance (NMR) spectrum show that no liquid product is produced (Fig. S14, ESI†). The faradaic efficiency for H_2 (FE_{H_2}) and (FE_{CO}) were recorded in the potential range from −0.6 V to −1.2 V. NNU-17 was employed as an electrocatalyst to split CO_2, and the maximum FE_{CO} can reach to 90.3% at −1.0 V (Fig. 2b and c). Even at the potential of −1.0 V and −1.1 V, FE_{CO} can still maintain above 85%. In a wide potential range from −0.9 V to −1.2 V, NNU-17 has relatively high selectivity and activity for CO_2 conversion instead of the H_2 evolution reaction (HER). In contrast to NNU-17 (−1.0 V, FE_{CO} ∼ 90.3%), the FE_{co} of NNU-18 favors at more negative potential (−1.1 V) reaching the maximum value of 82.1% (Fig. 2b and Fig. S15, ESI†). At −1.0 V, only around 62.5% of FE_{CO} was found for NNU-18 (Fig. 2c). Meanwhile, the TOF (CO) for NNU-18 at this potential is 189 h^{-1} lower than that of NNU-17 (353 h^{-1}) (Fig. S16, ESI†). The performance discrepancy between the two crystals may be due to the different coordination halide ions types. To verify the CO source during ECR reaction, the CO_2 atmosphere was replaced by the $^{13}CO_2$ atmosphere to perform isotopic experiments, and the generated gas was analyzed by gas chromatography-mass spectrometry (GC-MS) (Fig. 2d). ^{13}CO was found at the peak of m/z = 29, which fully proves that the reduction product comes from the reaction substrate ($^{13}CO_2$). In order to eliminate the influence of conductive substrates, the electrolysis reactions were carried out by performing carbon paper and acetylene black as control groups in various potentials. The conductive substrates do not produce CO, and almost only H_2 is produced at relatively high potentials (Fig. S17 and S18, ESI†). In addition, the maximum FE_{CO} of TIPP ligand is about 13.2% at −0.7 V, while there is only 2.6% at −1.0 V (Fig. S19, ESI†). It is further indicated that the catalytic sites of the catalysts mainly originate from the metal parts of the MOF.

To shed further light on the ECR performance of NNU-17 and NNU-18, the electrochemical double-layer capacitance (C_{dl}) recorded from the cyclic voltammogram (CV) curve was used to calculate electrochemically active surface area (ECSA). The C_{dl} of NNU-17 (13.19 mF cm^{-2}) is higher than that of NNU-18 (9.94 mF cm^{-2}), implying NNU-17 can provide more accessible surface in the reduction reaction (Fig. S20, ESI†). The partial CO current density (j_{CO}) was obtained by FE_{CO} and total current density. NNU-17 exhibits a larger j_{CO} (−8.8 mA cm^{-2}) at −1.0 V, almost twice than that of NNU-18 (−4.6 mA cm^{-2}) (Fig. S21, ESI†). The kinetic study of CO_2 electroreduction can be evaluated by Tafel slope based on Tafel equation, $\eta = b \log |j_{CO}| + a$, where b is the Tafel slope, η is the overpotential and j_{CO} is partial CO current density (Fig. S21c, ESI†). The Tafel slopes for NNU-17 and NNU-18 are 271 mV dec^{-1} and 305 mV dec^{-1} respectively, which indicates the favorable kinetics of NNU-17 for CO generation. Electrochemical impedance spectroscopy (EIS) experiments were conducted to evaluate the charge transfer resistance. The charge transfer resistance of NNU-17 is smaller than that of NNU-18, indicating that the shuttle of charge transfer on NNU-17 is faster. As a result, NNU-17 possesses the smaller ohmic loss, exhibiting the higher selectivity and activity than NNU-18 in ECR reaction (Fig. S22, ESI†).

Catalytic stability is an important parameter for both nano- or molecular catalysts. NNU-17 and NNU-18 show remarkable acid/alkali resistance under the wide pH condition. In order to further reveal the stability of NNU-17 and NNU-18 in the ECR process, the PXRD pattern of the catalysts after the electrolysis reaction was compared to that of the catalysts before test (Fig. S23, ESI†). The result reveals that crystal catalysts still maintain good stability even after the electrocatalytic reaction. The long-term stability of the catalyst is still one of the main challenges of ECR reaction. Thus, the current stability of NNU-17 and NNU-18 was continuously monitored at −1.0 V. After 30 h, it is stable over 10 mA cm^{-2} for NNU-17; after 35 h, the current density of NNU-18 is about 6.7 mA cm^{-2} (Fig. S24, ESI†). No significantly decreasing illustrates that both NNU-17 and NNU-18 maintain good current stabilities. The electrolyte after experiment was examined by inductively coupled plasma emission spectroscopy (ICP), ultraviolet-visible (UV-Vis) spectrophotometer and ion chromatography. The ICP analysis shows that Cd concentration is below the detection limit, further indicating that nothing is dissolved after the electroreduction reaction (Table S2, ESI†). UV-Vis spectra show there is no ligand dissolved in electrolyte after the ECR experiments (Fig. S25, ESI†). The ion chromatography analysis reveals that no halogen anion decomposes and releases from the catalyst into the electrolyte solution after ECR reaction (Fig. S26, ESI†).

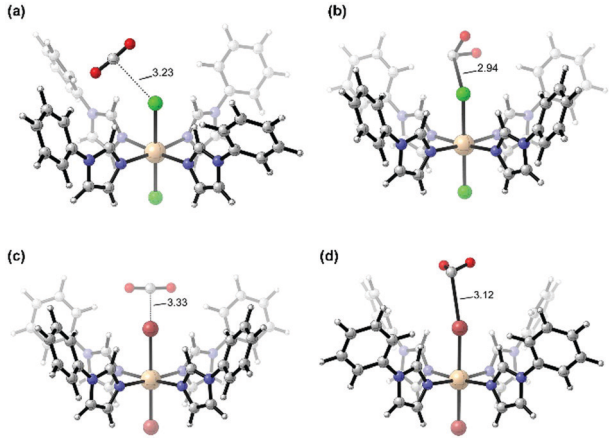

Fig. 3 DFT calculations for adsorption and activation of CO_2 in NNU-17 and NNU-18. (a) Initial and (b) optimized configuration are in Cl-coordinated NNU-17. (a) Initial and (b) optimized configuration are in Br-coordinated NNU-18.

These stability tests demonstrate that both NNU-17 and NNU-18 are stable crystal catalysts in the ECR reaction, acting as promising electrocatalysts in ECR reaction.

The performance differences in FE_{CO} selectivity and CO_2 adsorption capacity between the two crystal catalysts are mainly caused by different coordinated halogen ions. DFT calculations were performed to further explain the effect of halogen on the activity and reveal the catalytic reaction mechanisms of ECR. As shown in Fig. 3, the Cd2 site is saturated with six atoms, thus the attraction for CO_2 from the metal is limited due to the strong coordination interaction. However, the optimized structures show that CO_2 is non-linear, and the distance of C–Cl/C–Br is 2.94/3.12 Å (Fig. 3). This suggests that the coordination of halogen is beneficial for activation of CO_2. The calculated interaction energy between CO_2 and coordinated Cl^- is 1.88 kcal mol^{-1} higher than that generated between CO_2 and coordinated Br^- (Table S3, ESI†), which is corresponded to the better CO_2 adsorption capacity and ECR performance of NNU-17. Herein, the reduction route mainly includes: firstly, the adsorption and activation of CO_2 are accompanied by adsorption of a proton–electron pair, resulting in the formation *COOH species; with the subsequent electron and proton transfer, the *COOH is further reduced to generate *CO with removing water; finally, CO will be released from Cd1 sites. Among them, the axially coordinated halogen anions of Cd2 are mainly responsible for adsorption and activation of CO_2, the activated CO_2 molecules are further reduced into CO by the Cd1 ions in the center of porphyrin.

In conclusion, we synthesized two stable isostructural MOFs (NNU-17 and NNU-18) by replacing different halogen ions, further to study the effect of different halogen anions on ECR performance. NNU-17 exhibits a high FE_{CO} reaching to 90.3% at −1.0 V, while that of NNU-18 is only 62.5%. With the stronger electron-withdrawing capacity exhibits, Cl-coordinated NNU-17 shows the higher CO_2 adsorption capacity. Moreover, the DFT calculations reveal that the curved state of CO_2 can be induced by both the coordinated halogens, but with stronger CO_2 binding energy found on Cl^-. In total, we successfully established the crystal model to ameliorate ECR performance by utilizing different halogen anions to modulate the affinity between CO_2 and catalyst.

This work was financially supported by NSFC (No. 21622104, 21871141, 21871142 and 21701085), the NSF of Jiangsu Province of China (No. SBK2017040708), the Natural Science Research of Jiangsu Higher Education Institutions of China (No. 17KJB150025).

Conflicts of interest

There are no conflicts to declare.

Notes and references

1 M. G. Kibria, J. P. Edwards, C. M. Gabardo, C. T. Dinh, A. Seifitokaldani, D. Sinton and E. H. Sargent, *Adv. Mater.*, 2019, **31**, e1807166.
2 K. Ogura, J. R. Ferrell, III, A. V. Cugini, E. S. Smotkin and M. D. Salazar-Villalpando, *Electrochim. Acta*, 2010, **56**, 381–386.
3 A. S. Varela, W. Ju, T. Reier and P. Strasser, *ACS Catal.*, 2016, **6**, 2136–2144.
4 D. Gao, F. Scholten and B. Roldan Cuenya, *ACS Catal.*, 2017, **7**, 5112–5120.
5 M. Cho, J. T. Song, S. Back, Y. Jung and J. Oh, *ACS Catal.*, 2018, **8**, 1178–1185.
6 H. Q. Fu, L. Zhang, L. R. Zheng, P. F. Liu, H. Zhao and H. G. Yang, *J. Mater. Chem. A*, 2019, **7**, 12420–12425.
7 J. R. Long and O. M. Yaghi, *Chem. Soc. Rev.*, 2009, **38**, 1213–1214.
8 Q. Huang, Q. Li, J. Liu, Y. R. Wang, R. Wang, L. Z. Dong, Y. H. Xia, J. L. Wang and Y.-Q. Lan, *Matter*, 2019, **1**, 1656–1668.
9 L. Jiao, Y. Wang, H.-L. Jiang and Q. Xu, *Adv. Mater.*, 2018, **30**, 1703663.
10 Y. Bai, Y. Dou, L.-H. Xie, W. Rutledge, J.-R. Li and H.-C. Zhou, *Chem. Soc. Rev.*, 2016, **45**, 2327–2367.
11 A. Dhakshinamoorthy, Z. Li and H. Garcia, *Chem. Soc. Rev.*, 2018, **47**, 8134–8172.
12 C. A. Trickett, A. Helal, B. A. Al-Maythalony and Z. H. Yamani, *Nat. Rev. Mater.*, 2017, **2**, 17045.
13 C. S. Diercks, Y. Liu, K. E. Cordova and O. M. Yaghi, *Nat. Mater.*, 2018, **17**, 301–307.
14 A. Schoedel, Z. Ji and O. M. Yaghi, *Nat. Energy*, 2016, **1**, 16034.
15 N. Kornienko, Y. Zhao, C. S. Kiley, C. Zhu, D. Kim, S. Lin, C. J. Chang, O. M. Yaghi and P. Yang, *J. Am. Chem. Soc.*, 2015, **137**, 14129–14135.
16 S. Dou, J. Song, S. Xi, Y. Du, J. Wang, Z.-F. Huang, Z. J. Xu and X. Wang, *Angew. Chem., Int. Ed.*, 2019, **58**, 4041–4045.
17 I. Hod, M. D. Sampson, P. Deria, C. P. Kubiak, O. K. Farha and J. T. Hupp, *ACS Catal.*, 2015, **5**, 6302–6309.
18 S. Y. Reiko Hinogamiz, M. Deguchi, Y. Zenitani, H. Hashiba and Y. Yamada, *ECS Electrochem. Lett.*, 2012, **1**, H17–H19.
19 X. Jiang, H. Li, J. Xiao, D. Gao, R. Si, F. Yang, Y. Li, G. Wang and X. Bao, *Nano Energy*, 2018, **52**, 345–350.

